Slk19 enhances cross-linking of microtubules by Ase1 and Stu1

Sarina Norell, Jennifer Ortiz, and Johannes Lechner*
Biochemie-Zentrum der Universität Heidelberg, INF 328, 69120 Heidelberg, Germany

ABSTRACT **The *Saccharomyces cerevisiae* protein Slk19 has been shown to localize to kinetochores throughout mitosis and to the spindle midzone in anaphase. However, Slk19 clearly also has an important role for spindle formation and stabilization in prometaphase and metaphase, albeit this role is unresolved. Here we show that Slk19's localization to metaphase spindles in vivo and to microtubules (MTs) in vitro depends on the MT cross-linking protein Ase1 and the MT cross-linking and stabilizing protein Stu1. By analyzing a *slk19* mutant that specifically fails to localize to spindles and MTs, we surprisingly found that the presence of Slk19 amplified the amount of Ase1 strongly and that of Stu1 moderately at the metaphase spindle in vivo and at MTs in vitro. Furthermore, Slk19 markedly enhanced the cross-linking of MTs in vitro when added together with Ase1 or Stu1. We therefore suggest that Slk19 recruits additional Ase1 and Stu1 to the interpolar MTs (ipMTs) of metaphase spindles and thus increases their cross-linking and stabilization. This is in agreement with our observation that cells with defective Slk19 localization exhibit shorter metaphase spindles, an increased number of unaligned nuclear MTs, and most likely reduced ipMT overlaps.**

Monitoring Editor
Kerry Bloom
University of North Carolina, Chapel Hill

Received: Jun 1, 2021
Revised: Aug 27, 2021
Accepted: Aug 30, 2021

INTRODUCTION

The formation of a functional mitotic spindle is essential for the reliable segregation of chromosomes in eucaryotes. The spindle of higher eucaryotes consists of a high density of microtubules (MTs) that nucleate at various sites, such as centrosomes, chromosomes, or other MTs, and is organized by more than 1000 spindle proteins (Petry, 2016). In contrast, the mitotic spindle of *Saccharomyces cerevisiae* appears quite simple. The MTs are nucleated close to the spindle pole bodies (SPBs; the yeast centrosomes) that are embedded in the nuclear membrane. Astral MTs emanate from the cytosolic sides of the SPBs, whereas 16 kinetochore MTs (kMTs) and ~4 interpolar MTs (ipMTs) nucleate at the nuclear side of each SPB (Winey *et al.*, 1995). A MT minus-end-directed motor (Kar3/Cik1) facilitates the alignment of antiparallel ipMTs between the spindle poles either per se (Hepperla *et al.*, 2014) or in association with the MT plus end tracking protein Bim1 (Kornakov *et al.*, 2020) and plus-end-directed motors (Cin8 and Kip1) provide a force that slides the ipMTs apart (Saunders and Hoyt, 1992). Stu1, a protein that belongs to the CLASP family of MT rescue factors, is essential for the stabilization of the nuclear spindle MTs (Yin *et al.*, 2002) and also may contribute to the cross-linking of ipMTs up to metaphase (Funk *et al.*, 2014). In addition, Ase1, as its orthologs in other eucaryotes, cross-links ipMTs in metaphase and at the spindle midzone in anaphase (Schuyler *et al.*, 2003; Bieling *et al.*, 2010; Subramanian *et al.*, 2010).

Slk19 was originally identified as a centromere-associated protein that functions to stabilize the mitotic spindle (Zeng *et al.*, 1999). At the centromere, Slk19 contributes to the clustering of kinetochores (KTs) (Richmond *et al.*, 2013; Mittal *et al.*, 2019), to centromeric elasticity (Zhang *et al.*, 2006), and to the regulation of the activity of the separase Esp1 (Lianga *et al.*, 2018). Furthermore Slk19, together and interdependently with Stu1, is sequestered at unattached KTs (Kolenda *et al.*, 2018). This compromises the metaphase spindle and consequently allows the formation of long nuclear random MTs that can capture unattached KTs (Kolenda *et al.*, 2018). Slk19's role for the mitotic spindle was predominantly investigated in anaphase. First, Slk19 has a regulatory role as a member of the

This article was published online ahead of print in MBoC in Press (http://www.molbiolcell.org/cgi/doi/10.1091/mbc.E21-05-0279).

*Address correspondence to: Johannes Lechner (johannes.lechner@bzh.uni-heidelberg.de).

Abbreviations used: AID, auxin-induced degradation; AMCA, aminomethylcoumarin acetate; ChIP, chromatin immunoprecipitation; cc, coiled coil; CL, C-terminal loop; DTT, dithiothreitol; FEAR, Cdc14 early anaphase release; GD, globular domain; HRP, horseradish peroxidase; IAA, indole acetic acid; ipMT, interpolar microtubule; kMT, kinetochore microtubule; KT, kinetochore; MT, microtubule; nrMT, nuclear random microtubule; PBS, phosphate-buffered saline; PMSF, phenylmethylsulfonyl fluoride; SPB, spindle pole body; TACC, transforming acid coiled coil; WCE, whole-cell extract; WT, wild type.

FEAR (Cdc14 early anaphase release) pathway (Stegmeier *et al.*, 2002). After activation at anaphase onset, Esp1 together with Slk19 and Spo12 promote the partial release of the phosphatase Cdc14 from the nucleolus that dephosphorylates (among other proteins) Ase1 (Khmelinskii *et al.*, 2007). This facilitates the formation of a spindle midzone with sufficient Cin8 (Khmelinskii *et al.*, 2009) to slide the MTs apart and Stu2, a MT polymerase of the XMAP125 family (Podolski *et al.*, 2014), to elongate the gliding MTs (Severin *et al.*, 2001). Second, Slk19 itself localizes to the spindle midzone (Sullivan *et al.*, 2001) and there is evidence that Slk19 has a FEAR-independent role for anaphase spindle elongation (Havens *et al.*, 2010). Irrespective of its role for the anaphase spindle, Slk19 is clearly important for spindle formation from prometaphase to metaphase. Δ*slk19* cells arrested in metaphase exhibit considerably shorter spindles than wild type (*WT*) cells (Zeng *et al.*, 1999). Furthermore, Slk19 is **s**ynthetic **l**ethal with **K**ar3 and Δ*slk19 kar3-ts* double mutants arrest in metaphase with a defective spindle (Zeng *et al.*, 1999). However, it remained unclear how Slk19 contributes to the stability of metaphase spindles.

Here we show that Slk19 localizes to the overlap zone of metaphase spindles with a dependence on Stu1 and Ase1, and that Slk19 interacts with MT-bound Ase1 and Stu1 in vitro. Surprisingly, we find that Slk19 amplifies the localization of Ase1 and Stu1 to metaphase spindles and to MTs in vitro. Furthermore, presumably by increasing the load of Ase1 or Stu1, Slk19 enhances the cross-linking of MTs by these proteins in vitro. We thus suggest that Slk19 stabilizes metaphase spindles by enhancing the cross-linking and rescue of ipMTs via Ase1 and Stu1. This is in agreement with the phenotypes of Δ*slk19* cells and of a *slk19* mutant that is defective for metaphase spindle localization. These cells frequently exhibit unaligned MTs and spindles with altered overlap zones.

RESULTS

Slk19 localizes to the metaphase spindle

Slk19 plays an important role for the spindle throughout mitosis in *S. cerevisiae* (see above). For anaphase, the nature of this role is at least partially defined (Sullivan *et al.*, 2001; Stegmeier *et al.*, 2002; Khmelinskii *et al.*, 2007; Havens *et al.*, 2010; Faust *et al.*, 2013); for metaphase, it is not. To start with, it is unclear whether Slk19 localizes to the spindle MTs in metaphase, in contrast to anaphase, when Slk19 clearly localizes to the spindle midzone. In metaphase-arrested cells, Slk19 localizes to the cluster of sister KTs (Figure 1, A and B). We, however, found it difficult to claim unambiguously that Slk19 localizes to the metaphase spindle. Many metaphase-arrested cells showed a continuous Slk19 signal between the KT clusters but also a substantial number of cells exhibited at best a fragmented Slk19 signal (Figure 1A). In addition, we found that the strong KT signal of Slk19 could interfere with the observation of Slk19's spindle localization, particularly when the spindle size and distance between KT clusters is small. To circumvent this, we aimed to interfere with the KT localization while leaving a putative spindle localization intact. As published (Pagliuca *et al.*, 2009), the KT protein Spc105 may be involved in KT localization of Slk19 and indeed, Slk19 failed to localize to KTs when we depleted Spc105 ('Δ*spc105*') in metaphase-arrested cells (Figure 1, A and B; Supplemental Figure S1B). The interaction of Slk19 with Spc105 may be direct or indirect. For instance, Slk19 might interact with Kre28 that forms a stable complex with Spc105 (Pagliuca *et al.*, 2009) or with spindle assembly checkpoint components that assemble on Spc105 (London *et al.*, 2012; London and Biggins, 2014), particularly, Bub1 and Bub3 that likely reside on KTs even when KTs are bipolar attached (as in metaphase-arrested cells) (Gillett *et al.*, 2004). Importantly, however, after interfering with its KT localization, Slk19 could be clearly detected between the sister KT clusters but not between the sister KTs and the corresponding spindle poles in Spc105-depleted cells (Figure 1A). This indicates that Slk19 specifically localizes to overlapping ipMTs, but not strongly to the remaining part of the ipMTs and not strongly to the kMTs in these cells.

Interestingly, the spindle localization of Slk19 appears to be increased in Spc105-depleted cells in comparison to the (putative) localization in *WT* cells (Figure 1B). This effect, however, is not restricted to cells depleted of Spc105. Cells that express Stu1 lacking its TOGL1 domain (Figure 1C) that confers Stu1 KT localization and kMTs stabilization (Funk *et al.*, 2014), also exhibit particularly strong spindle localization of Slk19 (Supplemental Figure S1A). Common to these cells and Spc105-depleted cells is that in both the kMTs are shorter than in *WT* cells (Supplemental Figure S1C). Since this effect is not sufficiently compensated by the small reduction in spindle length, the KT clusters in Spc105-depleted and Stu1ΔTOGL1-expressing cells are at a greater distance than in *WT* cells (Supplemental Figure S1C). Thus, the KTs of these cells are likely to experience higher tension than those of *WT* cells and this apparently correlates with a stronger spindle localization of Slk19 (see also *Discussion*).

A coiled-coil (cc) region of Slk19 is essential for the localization to the metaphase spindle

To investigate the role of Slk19 for the metaphase spindle, we aimed to identify a Slk19 mutant that was defective for metaphase spindle localization but not for KT localization. Slk19 has been reported to form a homotetramer (De Wulf *et al.*, 2003). To be able to address whether a particular localization defect might be due to defective tetramerization, we first determined the Slk19 region required for Slk19–Slk19 interaction. We thus investigated the coimmunoprecipitation of a GFP-tagged *WT* Slk19 with a FLAG-tagged deletion mutant form. According to Havens *et al.* (2010) and further secondary structure analysis, Slk19 is predicted to contain an N-terminal globular domain (GD) and seven cc regions (cc1–7) (Figure 2A). Deletion of the GD, cc1+2, or cc3–5 did not compromise Slk19–Slk19 interaction (Figure 2B). In contrast, the deletion of cc6+7 abolished Slk19–Slk19 interaction completely. Furthermore, *WT* Slk19 copurified very efficiently with only cc6+7 (*slk19Δaa1-708*). We thus conclude that cc6+7 is essential and sufficient for Slk19–Slk19 interaction and thus essential for tetramerization. Deletion of cc6+7 abolished the localization of Slk19 to KTs in metaphase (Figure 2C) and anaphase (Figure 2E) to the metaphase spindle (Figure 2C) and anaphase midzone (Figure 2E). Conversely, cc6+7 (*slk19Δaa1-708*) alone localized to KTs (Figure 2, C and E), but not to the metaphase spindle (Figure 2D) or the anaphase midzone (Figure 2E). Thus cc6+7 confers KT localization. Tetramerization may or may not be required in this case. On the other side, cc6+7 is necessary but not sufficient for spindle localization. It thus is likely that the localization of Slk19 to the metaphase spindle or anaphase midzone requires tetramerization. Deletion of the N-terminal GD, cc2 or cc3–5 did not abolish the localization to KTs (Figure 2, C and E), the metaphase spindle (Figure 2D), or the anaphase midzone (Figure 2E). Deletion of cc1 also did not abolish KT localization (Figure 2C) but resulted in a severe localization defect to the metaphase spindle (Figure 2D) and the anaphase midzone (Figure 2E). Importantly, the cellular level of Slk19Δcc1 (and Slk19Δcc6+7) was at least as high as that of *WT* Slk19 in metaphase-arrested cells after Spc105 depletion (Supplemental Figure S2). Thus, the compromised spindle localization of Slk19Δcc1 is not due to diminished expression or increased instability of Slk19Δcc1. Taken together, *slk19Δcc1* mutants therefore

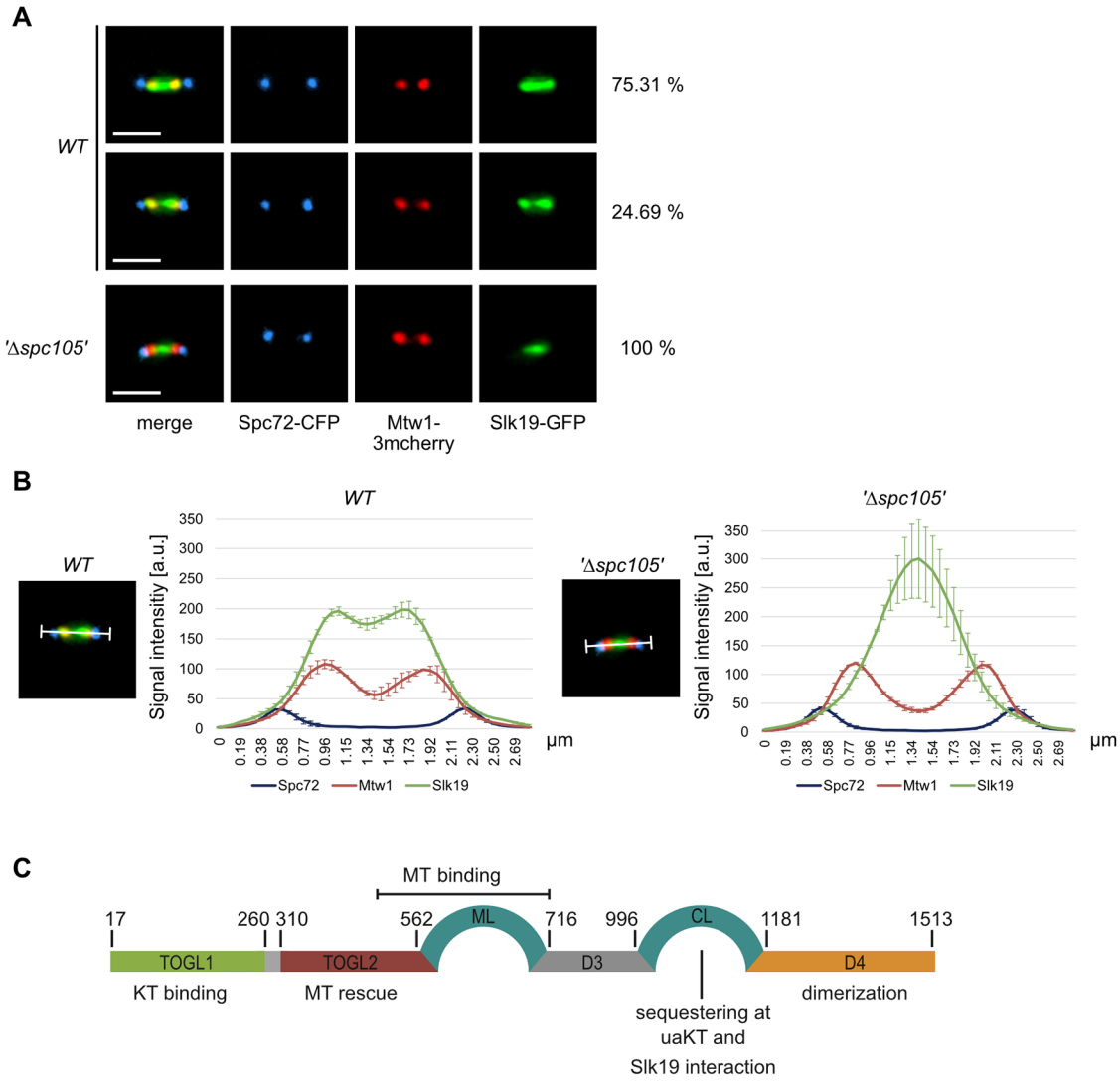

FIGURE 1: Slk19 localizes to metaphase spindles. (A, B) Statistics see Supplemental Table S4. (A) Cells were arrested in metaphase by Cdc20 depletion (*GAL1* promoter shutoff). Subsequent Spc105 depletion ('Δ*spc105*') was performed as indicated (AID-system) to interfere with KT localization of Slk19. The percentage of cells revealing the depicted phenotype is indicated. Genotypes of the strains with the indicated fusion proteins are listed in Supplemental Table S1. Bars, 2 μm. (B) Cells were treated as in A. Mean distribution of the indicated proteins along the horizontal spindle axes (longitudinal blots in *Materials and Methods*). Vertical bars indicate the SD of two independent experiments. (C) Domain organization of Stu1 as shown in (Kolenda *et al.*, 2018).

appear particularly suitable to understand the role of Slk19 for the metaphase spindle.

Defective stability and alignment of ipMTs correlates with a failure of Slk19 to localize to metaphase spindles

Metaphase spindles are at average clearly shorter in Δ*slk19* cells than in *WT* cells (Zeng *et al.*, 1999) (Figure 3A). In more detail and similar to Zhang *et al.* (2006), we found that there is considerable variation in metaphase spindle sizes in Δ*slk19* cells (Figure 3A) ranging from a small number of average *WT* sizes (2–3 μm) to a large number of very short sizes (0.5–2 μm) (Figure 3A). Furthermore, there is an increased number of nuclear random MTs (nrMTs) in metaphase-arrested Δ*slk19* cells, as we reported earlier (Kolenda *et al.*, 2018) (Figure 3A), as well as in not-arrested prometaphase cells (Figure 3B). These nrMTs were clearly not aligned with MTs in the spindle axes and, at least in metaphase-arrested cells, appeared predominantly in correlation with short spindles (Figure 3A). Importantly, we found that this Δ*slk19* phenotype is identical to the *slk19*Δ*cc1* phenotype (Figure 3A). Thus, the frequent occurrence of short spindles and nrMTs that likely reflects defective MT stability and alignment correlates with the absence of Slk19 on metaphase spindles and is not the result of missing KT localization.

Localization of Slk19 to metaphase spindles is dependent on Stu1 and Ase1

As mentioned above, Slk19 localizes particularly in a region of the metaphase spindle where the overlap of ipMTs is expected to be maximal. This reflects the localization of Ase1 and Stu1, two proteins that are thought to cross-link ipMTs (Bieling *et al.*, 2010; Funk *et al.*, 2014). We thus wondered whether Slk19 localizes to metaphase spindles via these proteins. Cells depleted of Stu1 ('Δ*stu1*') during a metaphase arrest still showed Slk19 colocalizing with KTs (Figure 4A). But after depletion of Stu1 and Spc105, Slk19 only showed a diffuse nuclear staining in most cells (Figure 4A). However,

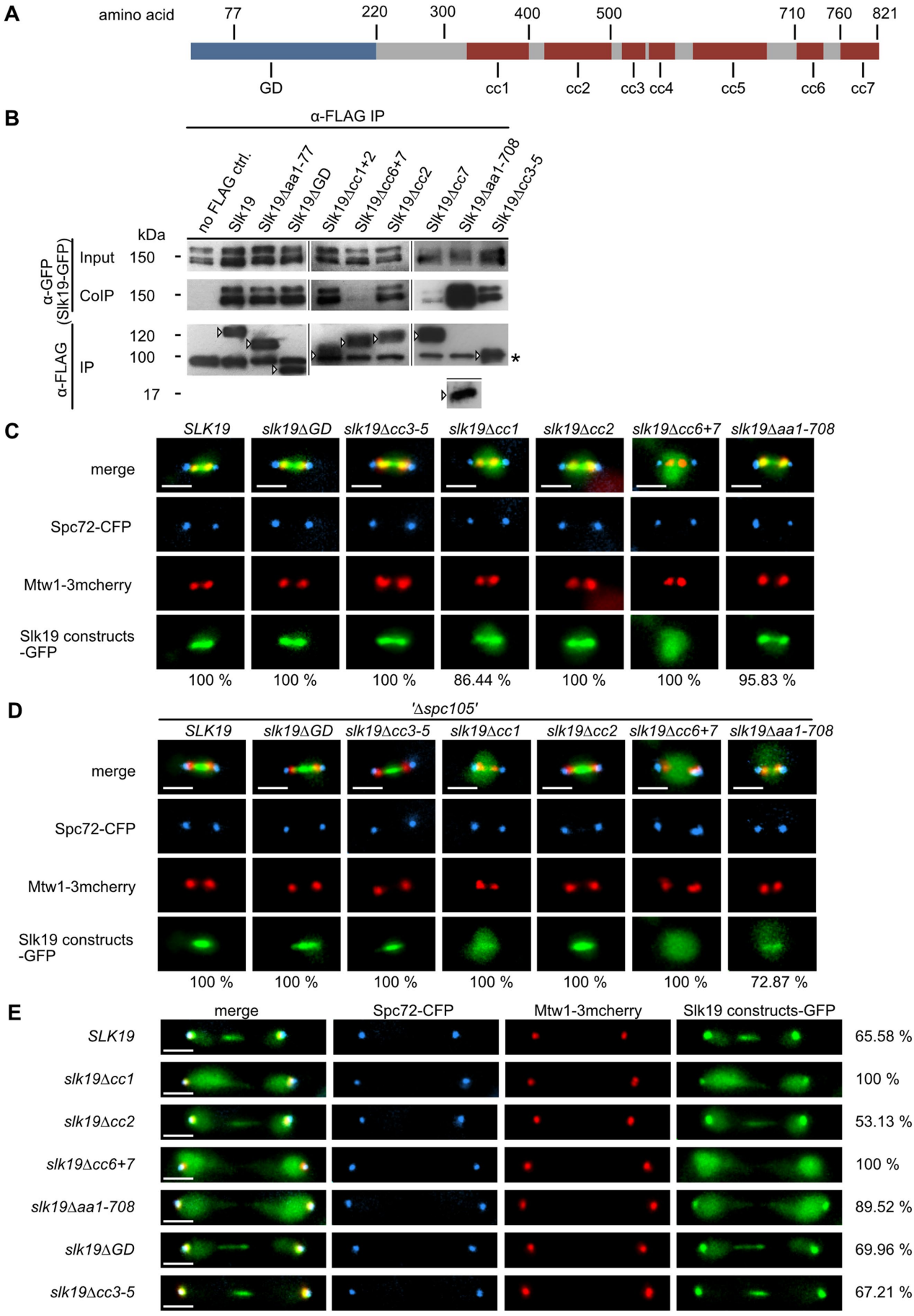
A
amino acid
77
220
300
400
500
710
760
821
GD
cc1
cc2
cc3
cc4
cc5
cc6
cc7
B
α-FLAG IP
no FLAG ctrl.
Slk19
Slk19Δaa1-77
Slk19ΔGD
Slk19Δcc1+2
Slk19Δcc6+7
Slk19Δcc2
Slk19Δcc7
Slk19Δaa1-708
Slk19Δcc3-5
kDa
α-GFP (Slk19-GFP)
Input
150
CoIP
150
α-FLAG
IP
120
100
17
*
C
SLK19
slk19ΔGD
slk19Δcc3-5
slk19Δcc1
slk19Δcc2
slk19Δcc6+7
slk19Δaa1-708
merge
Spc72-CFP
Mtw1-3mcherry
Slk19 constructs -GFP
100 %
100 %
100 %
86.44 %
100 %
100 %
95.83 %
D
'Δspc105'
SLK19
slk19ΔGD
slk19Δcc3-5
slk19Δcc1
slk19Δcc2
slk19Δcc6+7
slk19Δaa1-708
merge
Spc72-CFP
Mtw1-3mcherry
Slk19 constructs -GFP
100 %
100 %
100 %
100 %
100 %
100 %
72.87 %
E
merge
Spc72-CFP
Mtw1-3mcherry
Slk19 constructs-GFP
SLK19
65.58 %
slk19Δcc1
100 %
slk19Δcc2
53.13 %
slk19Δcc6+7
100 %
slk19Δaa1-708
89.52 %
slk19ΔGD
69.96 %
slk19Δcc3-5
67.21 %

these cells also had a very compromised spindle and thus the absence of Slk19 localization in these cells might be a consequence of just that. We, therefore, analyzed *stu1ΔCL* cells that lack a putatively unstructured region of Stu1 named the C-terminal loop (CL) (Figure 1C; Funk *et al*., 2014). Since *stu1ΔCL* cells fail to cosequester Slk19 to unattached KTs (Kolenda *et al*., 2018), we suspected that CL provides a Slk19 interaction domain. Furthermore, *stu1ΔCL* cells form metaphase spindles that are at least as long as that of *WT* cells (Funk *et al*., 2014) and have no increased number of nrMTs (Kolenda *et al*., 2018). Slk19 localization to *stu1ΔCL* spindles was substantially reduced in comparison to *WT* spindles (Figure 4A). Furthermore, Slk19 from metaphase-arrested cells copurified with *WT* Stu1 but failed to copurify with Stu1ΔCL (Figure 4C). We thus conclude that Slk19 localizes to the metaphase spindle partially via Stu1 and that the CL region of Stu1 is important for the Stu1–Slk19 interaction.

Ase1 localized to *stu1ΔCL* spindles (Figure 4A). Thus, the partial localization of Slk19 to metaphase spindles observed in *stu1ΔCL* cells (Figure 4A) might be conferred via Ase1. Deletion of *ASE1* in Spc105-depleted *STU1 WT* cells compromised the Slk19 localization to metaphase spindles substantially (Figure 4, A and B), whereas deletion of *ASE1* in Spc105-depleted *stu1ΔCL* cells abolished the Slk19 localization completely (Figure 4, A and B). We thus conclude that Stu1 and Ase1 synergistically localize Slk19 to metaphase spindles. In contrast to Stu1, we were, however, not able to copurify Ase1 with Slk19 from metaphase-arrested cells. The interaction of Slk19 with Ase1 may thus be less stable than the one with Stu1.

Intriguingly, *stu1ΔCL Δase1* cells do not show the short spindle phenotype of *Δslk19* cells, although Slk19 localization to the spindle is not observable in these cells. Consistently, *stu1ΔCL Δslk19* cells also do not exhibit a short spindle phenotype (Figure 4A). In metaphase-arrested *stu1ΔCL* cells, the kMTs and ipMTs are longer than in *WT* cells and the average distance between the separated KT clusters is smaller (Funk *et al*., 2014). Thus, Stu1ΔCL apparently stabilizes MTs more than *WT* Stu1 and this may compensate for some of the spindle defects caused by the absence of Slk19 (see also *Discussion*).

Slk19 enhances the amount of Ase1 and Stu1 at metaphase spindles

The metaphase spindle localization of Slk19 depends on Stu1 and Ase1. We wondered whether Slk19 would inversely influence the metaphase spindle localization of Ase1 and Stu1. Since short metaphase spindles (0.5–2 µm) prevail in *Δslk19* or *slk19Δcc1* cells and longer ones (2–3 µm) in *WT* cells, we compared larger and shorter *Δslk19* or *slk19Δcc1* spindles with *WT* spindles of corresponding sizes to make our data most consistent. Surprisingly, the level of Ase1 observed at metaphase spindles was dramatically reduced in *Δslk19* and *slk19Δcc1* cells in comparison to *WT* cells (Figure 5, A and B). Notably, Western analysis also revealed reduced cellular Ase1 levels in metaphase-arrested *slk19Δcc1* and *Δslk19* cells in comparison to *WT* cells (Figure 5, C and D). It is currently unclear whether this reflects reduced Ase1 expression or stability. If the latter is true, it could be due to lacking Slk19 interaction and spindle localization. It would then be the consequence and not the cause of diminished spindle localization. In any case, the reduction in cellular Ase1 levels clearly does not match the reduction in spindle localization of Ase1. Also, the localization of Stu1 at metaphase spindles was substantially reduced in *Δslk19* and *slk19Δcc1* cells (Figure 5, A and B). In contrast to Ase1, the cellular levels of Stu1, however, were very similar in metaphase-arrested *Δslk19* and *WT* cells (Figure 5, C and D). Thus, Stu1–Slk19 interaction is not required to maintain Stu1 stability. The described effects were very similar for shorter and longer spindles and could be rescued by reintroducing a *WT SLK19* copy at the *LYS2* locus of *Δslk19* or *slk19Δcc1* cells (Figure 5, A and B). Notably, the latter not only rescued but also increased the spindle localization of Ase1 and Stu1 above *WT* levels. We speculate that this could be the result of Slk19 overexpression that may occur if Slk19 expression at the *LYS2* locus is enhanced in comparison to the native *SLK19* locus or if multiple copies of *SLK19* were integrated at the *LYS2* locus. Taken together, we thus conclude that Slk19 enhances the localization of Ase1 and, to a lesser extent, Stu1 to metaphase spindles.

Δslk19 and *slk19Δcc1* spindles exhibit a diminished number of MTs at their center and altered Ase1 and Stu1 distribution

The cumulative tubulin signal of metaphase spindles was moderately reduced in *Δslk19* and *slk19Δcc1* cells in comparison to *WT* cells (Figure 5, A and B). In addition, averaging scans of individual cells along the spindle axes (longitudinal plots, see *Materials and Methods*) or orthogonal to the spindle axes at the midpoint between the two spindle poles (cross-section plots, see *Materials and Methods*) revealed that the tubulin signal was more reduced at the spindle center in *Δslk19* and *slk19Δcc1* cells than in *WT* cells (Figure 6, A and B). This conforms with a reduced number of MTs or MT overlaps in that region.

Longitudinal scans revealed that the localization of Ase1 and even Stu1 (that also localizes to KTs) maximizes at the spindle center in most (individual) *WT* cells (Figure 6, C and D). In *Δslk19* cells, however, the maximum of the (residual) Ase1 localization was frequently acentric and the Stu1 localization frequently displayed no defined maximum. If Ase1 is the predominant marker for MT overlaps, this may indicate that MT overlaps do not occur synchronously at the spindle center in *Δslk19* cells, and that Stu1 may not localize preferentially to overlaps as in *WT* cells (see also *Discussion*).

Slk19 binds to MTs via Ase1 or Stu1 in vitro

The in vivo experiments strongly indicated that Slk19 binds to MTs via Ase1 and Stu1 but not per se. We confirmed this in vitro.

FIGURE 2: Slk19 deletion analysis. (A) Putative structural organization of Slk19 according to (Havens *et al*., 2010) and additional secondary structure analysis (PSIPRED). GD, globular domain; cc, coiled-coil. (B–E) Genotypes of the strains with the indicated fusion proteins are listed in Supplemental Table S1. All *SLK19* deletion constructs were expressed from the endogenous *SLK19* promoter. (B) cc6+cc7 confers Slk19–Slk19 interaction. FLAG-tagged Slk19 constructs were coexpressed in *S. cerevisiae* with Slk19-GFP and affinity purified. Proteins were detected by Western analysis. Arrowheads indicate the different Slk19 deletion constructs. The asterisk indicates a background band. (C–E) The percentage of cells revealing the depicted phenotype is indicated. Statistics see Supplemental Table S4. Bars, 2 µm. (C, D) Cells were arrested in metaphase by Cdc20 depletion (*GAL1* promoter shutoff). (C) cc6+7 is essential for KT and spindle localization of Slk19 in metaphase. (D) cc1 is essential for spindle localization in metaphase. Spc105 depletion ('*Δspc105*') was used to interfere with KT localization of Slk19 (AID-system). (E) cc1 is essential for midzone localization of Slk19 and cc6+7 is essential for midzone and KT localization of Slk19 in anaphase. Cells were analyzed 2–2.5 h after release from a G1 arrest.

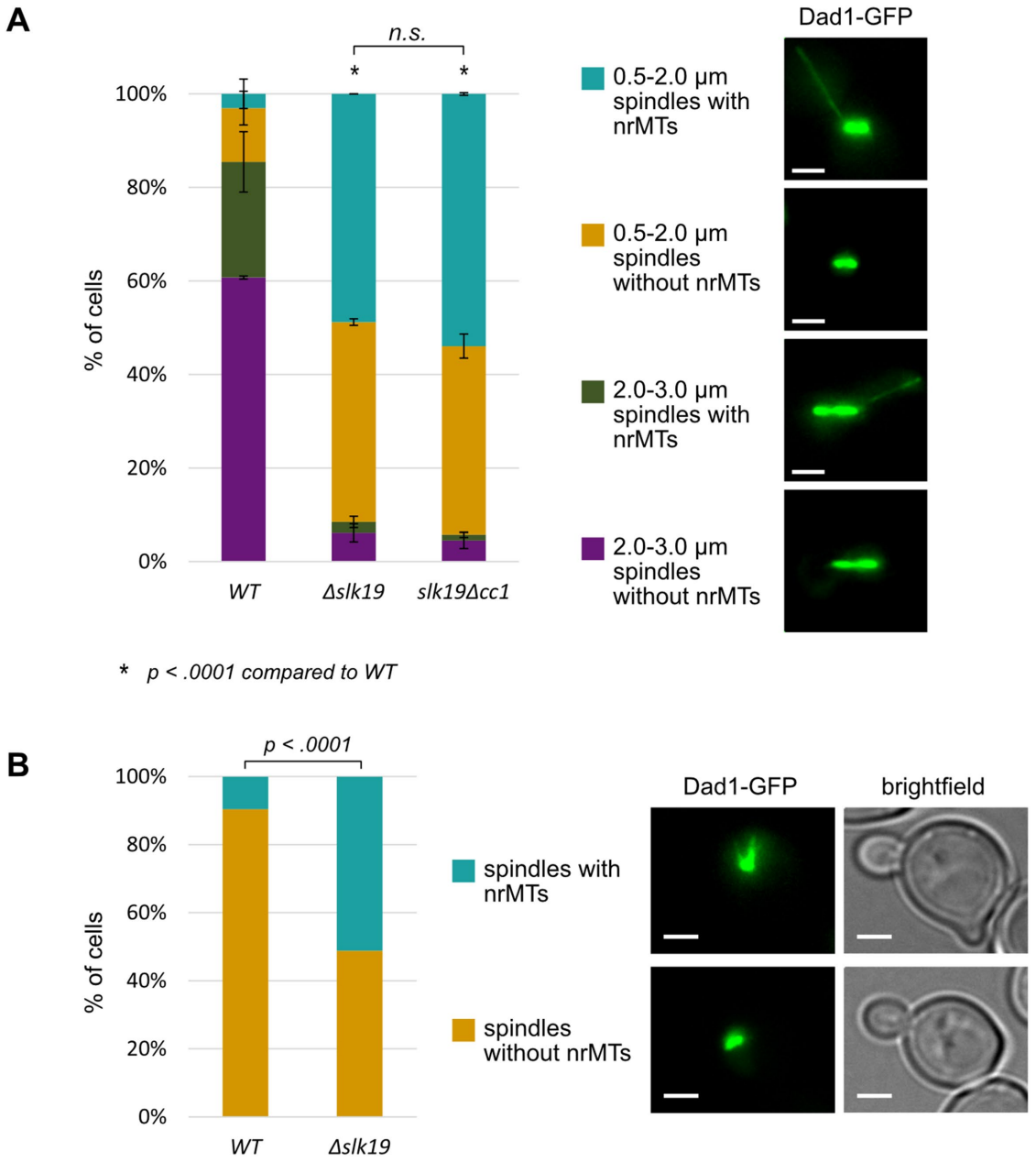

FIGURE 3: Δ*slk19* and *slk19*Δ*cc1* cells exhibit a highly increased number of short spindles and not-aligned nuclear MTs. (A and B) Nuclear MTs were visualized via Dad1-GFP localization. nrMTs, nuclear random MTs. n.s., not significant. Statistics see Supplemental Table S4. Bars, 2 µm. (A) Cells were arrested in metaphase by Cdc20 depletion (*MET25* promoter shutoff). Slk19Δcc1 was expressed from the endogenous *SLK19* promoter. (B) Cells were analyzed ~90 min after release from G1. Only cells with bud diameters ranging from 1.9–2.8 µm were included in the quantification.

Slk19-GFP, Slk19Δcc1-GFP, Ase1-3mCherry, and Stu1-CFP were purified as FLAG-tagged proteins from *S. cerevisiae* (Figure 7A) and incubated with taxol-stabilized, immobilized MTs in flow chambers. In contrast to Ase1 or Stu1, no direct binding of Slk19 to MTs could be detected (Figure 7B). However, Slk19 clearly bound to MTs that had been previously loaded with Ase1 or Stu1 (Figure 7C). Slk19 thereby colocalized with Ase1 or Stu1. Importantly, and in agreement with the in vivo experiments, Slk19Δcc1 failed to bind to MTs coated with Ase1 or Stu1 (Figure 7C).

As with other experiments that use proteins purified from an endogenous source (Mieck *et al.*, 2015), it is possible that contaminating or copurifying proteins present in our preparations in trace amounts might contribute the observed effects. These proteins would then copy the effects observed in vivo including the defective spindle interaction of Slk19Δcc1 and thus might even have an unknown spindle function. We consider this scenario as unlikely but cannot completely exclude it.

Slk19 amplifies the Ase1 and Stu1 localization to MTs in vitro

In vivo, the localization of Ase1 and Stu1 to metaphase spindles was diminished in Δ*slk19* and *slk19*Δ*cc1* cells. To test, whether Slk19 has an effect on the localization of Ase1 and Stu1 to MTs in vitro, we incubated MTs with Ase1 or Stu1 alone (as in Figure 7B) or in combination with Slk19 (Figure 7D). On incubation with an Ase1/Slk19 combination, the fluorescence signal of Ase1 at MTs increased

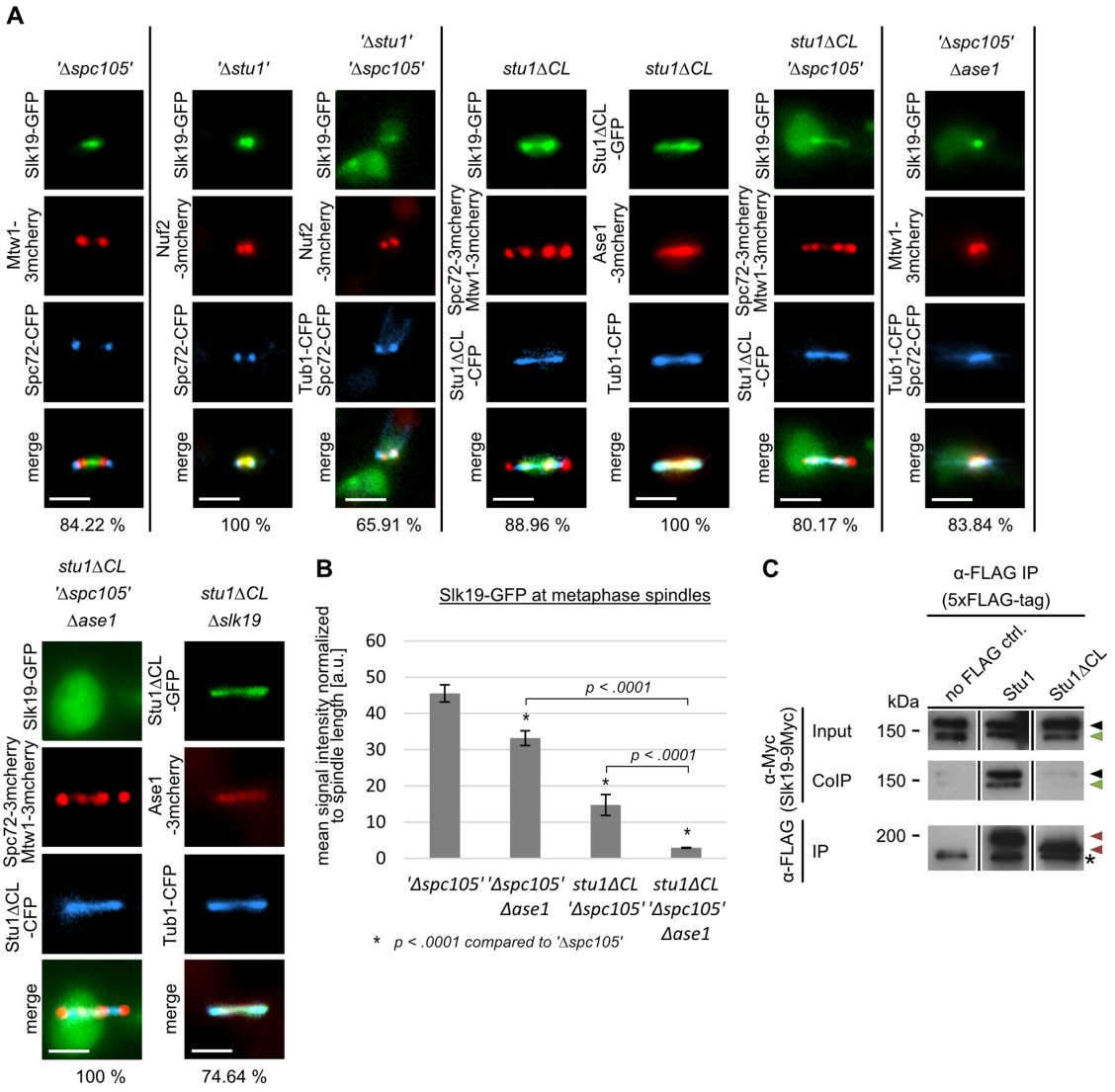

FIGURE 4: Slk19 localizes to metaphase spindles via Ase1 and the CL domain of Stu1. (A-C) Statistics see Supplemental Table S4. (A) Cells were arrested in metaphase by Cdc20 depletion (*MET25* or *GAL1* promoter shutoff). Spc105 depletion ('Δ*spc105*') was used to interfere with KT localization of Slk19 (AID-system). The '*Δspc105*' data from Figure 1A were included for better comparison. Genotypes of the strains with the indicated fusion proteins are listed in Supplemental Table S1. The percentage of cells revealing the depicted phenotype is indicated. Bars, 2 µm. (B) Quantification of Slk19 at metaphase spindles in indicated cells. The SD of two independent experiments are shown. (C) Slk19-Stu1 interaction in metaphase requires the CL domain of Stu1. Western analysis of affinity purified Stu1 constructs and copurifying Slk19. Black arrowheads mark full-length Slk19; green arrowheads mark a naturally occurring cleavage product of Slk19 (Sullivan *et al.*, 2001) and red arrowheads indicate FLAG-Stu1 or FLAG-Stu1ΔCL. The asterisk indicates a background band.

~4-fold in comparison to incubation with Ase1 alone (Figure 7E). On incubation with a Stu1/Slk19 combination, the Stu1 signal at MTs increased 1.7-fold in comparison to incubation with Stu1 alone (Figure 7E). Thus, Slk19 also amplifies the Ase1 and Stu1 localization at MTs in vitro, possibly via Ase1-Slk19-Ase1 or Stu1–Slk19-Stu1 interactions.

Slk19 enhances MT cross-linking via Ase1 or Stu1 in vitro

Since Δ*slk19* and *slk19Δcc1* cells exhibited phenotypes that indicated compromised cross-linking of ipMTs, we tested whether Slk19 has an effect on MT cross-linking in vitro. We first immobilized taxol-stabilized rhodamine-labeled MTs via biotin in neutravidin-coated flow chambers, incubated the chambers with the corresponding protein(s), and finally added mobile (biotin-free) aminomethylcoumarin acetate (AMCA)-labeled MTs. As a value for MT cross-linking, we then determined the sum of all rhodamine MT lengths that colocalized with AMCA-labeled MTs and normalized this value to the sum of all rhodamine-labeled MT lengths present in the examined micrographs (Figure 8A and *Materials and Methods*). We found that Slk19 cannot cross-link MTs in vitro, whereas Ase1 and Stu1 can, as has been described before (Bieling *et al.*, 2010; Funk *et al.*, 2014) (Figure 8, B and C). It is unclear why Stu1 appears to cross-link MTs more efficiently than Ase1 in our in vitro assay. However, we did observe that the preincubation of the immobilized MTs with a combination of Ase1 and Slk19 or Stu1 and Slk19 increased the colocalization (cross-linking) of immobilized and mobile MTs by a factor of 3 and 2.5, respectively, in comparison to preincubation with Ase1

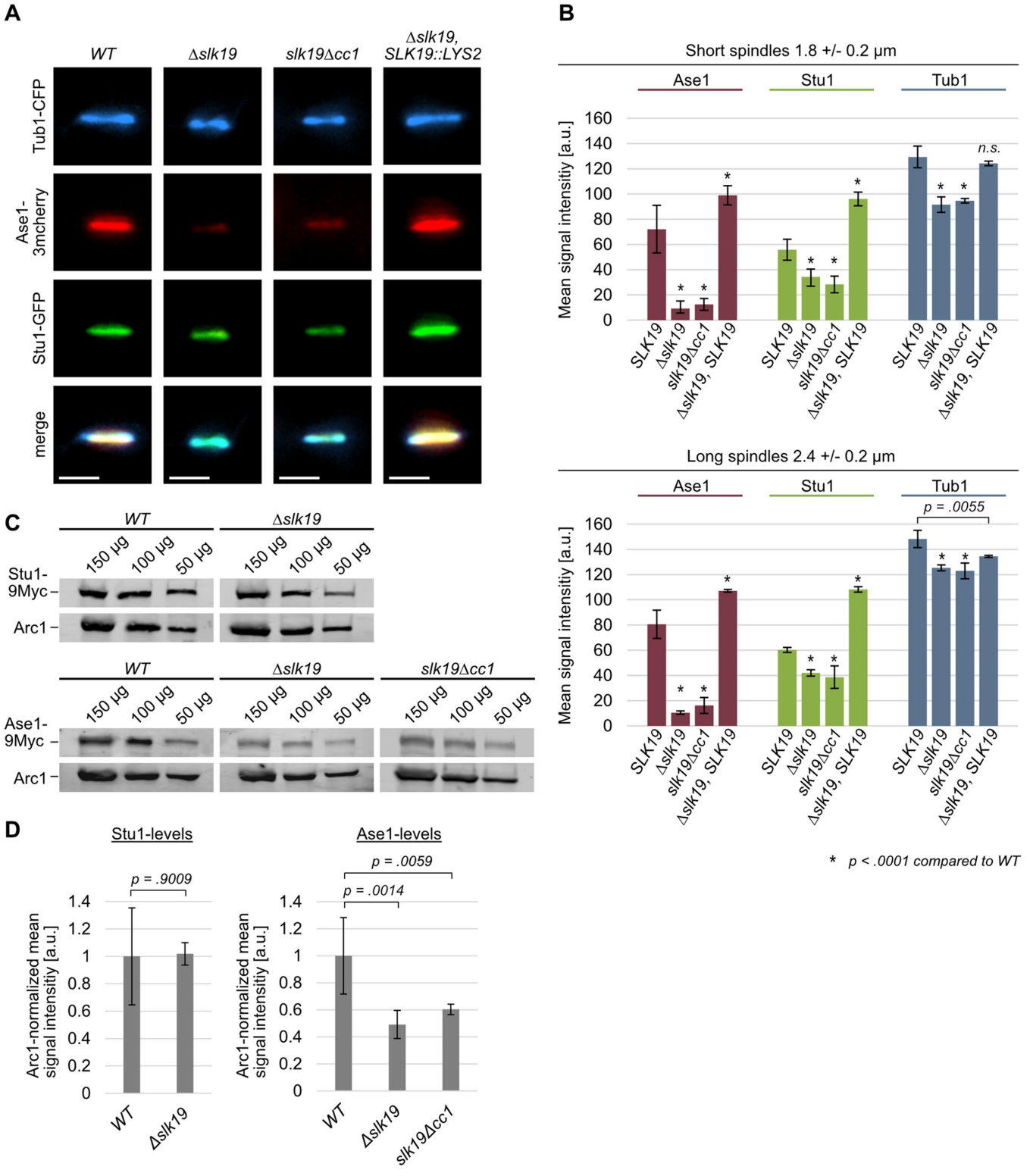

FIGURE 5: Slk19 amplifies the localization of Ase1 and Stu1 to metaphase spindles. (A–D) Genotypes of the strains with the indicated fusion proteins are listed in Supplemental Table S1. *SLK19* constructs were expressed from the endogenous *SLK19* promoter. (A) Example micrographs. Cells were arrested in metaphase by Cdc20 depletion (*MET25* promoter shutoff). Bars, 2µm. (B, D) The SD of two independent experiments is shown. Statistics see Supplemental Table S4. (B) Quantification of Ase1, Stu1, and Tub1 at metaphase spindles as shown in A; n.s., not significant. (C) Cellular levels of Ase1 and Stu1. Western analysis of WCEs with the indicated amounts of total protein. Detection with anti-Myc or anti-Arc1 antibody. (D) Quantification of Western results shown in C. *WT* values were set to "1."

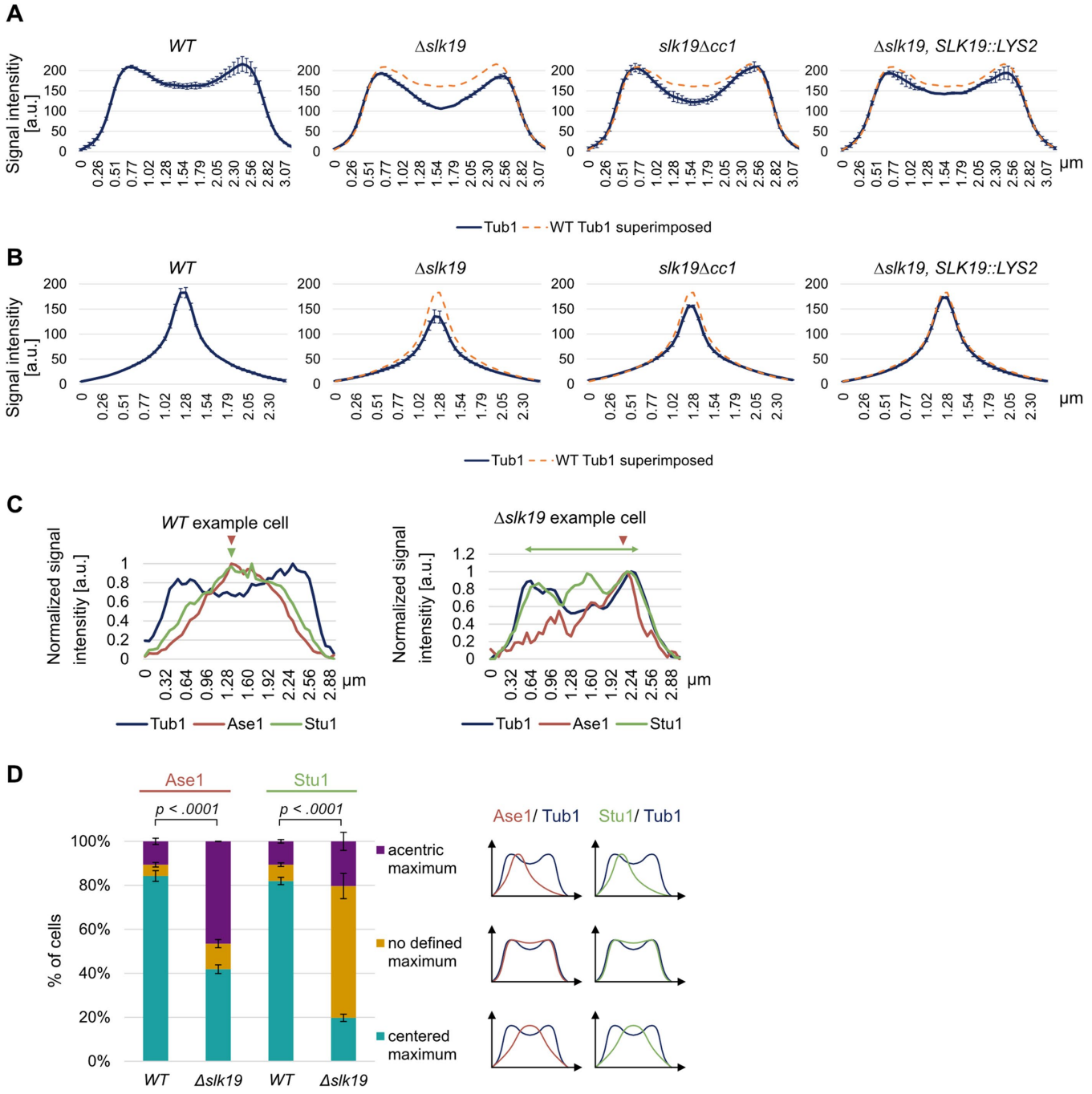

FIGURE 6: Slk19 synchronizes the overlap of ipMTs at the center of metaphase spindles. (A–D) Genotypes of the strains with the indicated fusion proteins are listed in Supplemental Table S1. Statistics see Supplemental Table S4. Cells were arrested in metaphase by Cdc20 depletion (*MET25* promoter shutoff). (A, B) *SLK19* constructs were expressed from the endogenous *SLK19* promoter. (A) Mean tubulin distribution along the metaphase spindle axes (see longitudinal blots in *Materials and Methods*). The vertical bars represent the SD of two independent experiments. The *WT* result is superimposed in the other blots for better comparison. (B) Mean tubulin distribution perpendicular (y-axes) to the spindle axes (x-axes) at the spindle center (see cross-section blots in *Materials and Methods*). The vertical bars represent the SD of two independent experiments. The *WT* result is superimposed in the other blots for better comparison. (C) Single cell examples of the distribution of Tub1, Ase1 and Stu1 along the spindle axes. Arrowheads indicate defined maxima and double headed arrows the lack of defined maxima. Note that for each protein, the maximal value was normalized to 1 so that the Ase1 distribution of the Δ*slk19* cells can be presented in one blot together with the distribution of Stu1 and Tub1. (D) Quantification of the distribution phenotypes of Ase1 and Stu1 in individual cells, as depicted in the cartoons.

or Stu1 alone (Figure 8, B and C). Preincubation of Ase1 or Stu1 with Slk19Δcc1 did not result in increased cross-linking. Taken together, this implies that Slk19 enhances MT cross-linking via Ase1 or Stu1, possibly as a result of the increased MT localization of Ase1 or Stu1 when MTs are incubated with a combination of Ase1 and Slk19 or Stu1 and Slk19.

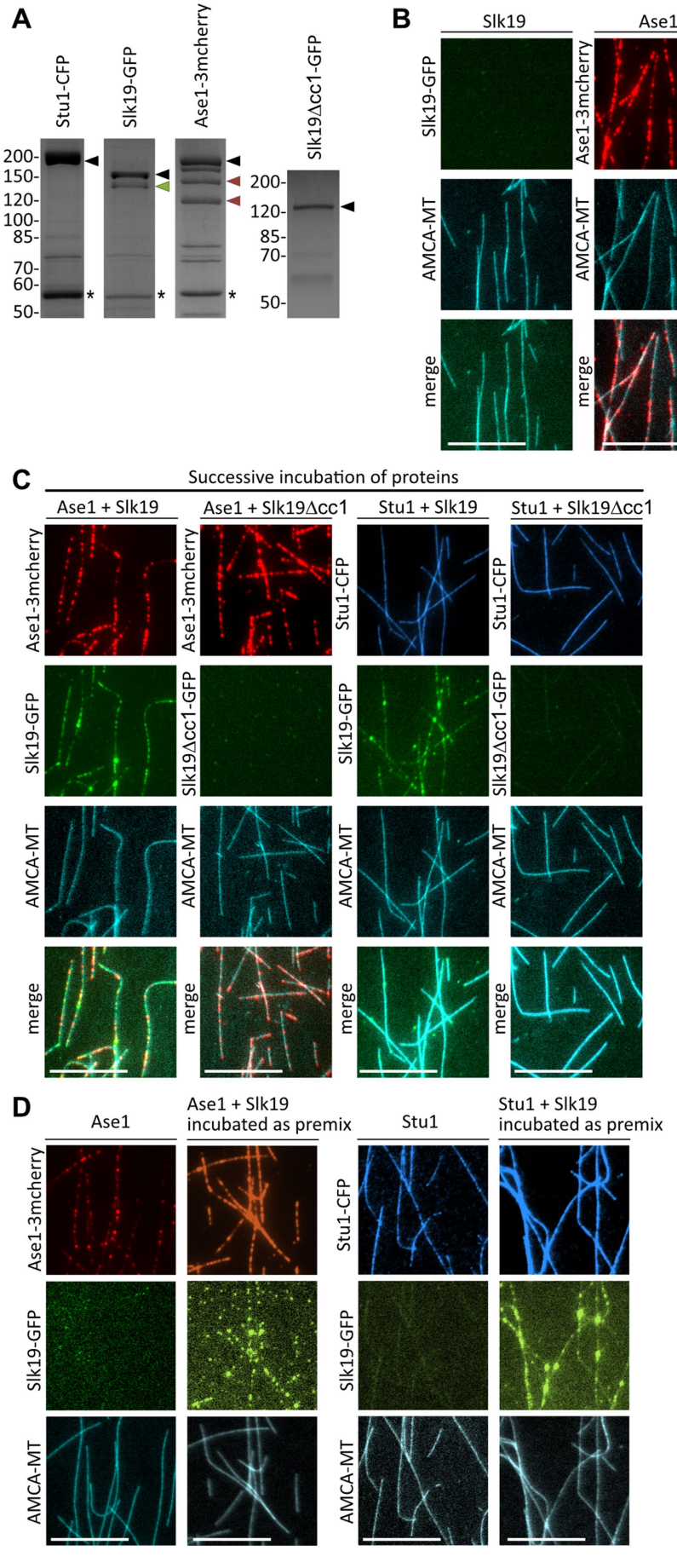
A
Stu1-CFP
Slk19-GFP
Ase1-3mcherry
Slk19Δcc1-GFP
200-
150-
120-
100-
85-
70-
60-
50-
B
Slk19
Ase1
Stu1
Slk19-GFP
Ase1-3mcherry
Stu1-CFP
AMCA-MT
merge
C
Successive incubation of proteins
Ase1 + Slk19
Ase1 + Slk19Δcc1
Stu1 + Slk19
Stu1 + Slk19Δcc1
Ase1-3mcherry
Stu1-CFP
Slk19-GFP
Slk19Δcc1-GFP
AMCA-MT
merge
D
Ase1
Ase1 + Slk19 incubated as premix
Stu1
Stu1 + Slk19 incubated as premix
E
Ase1 signal intensity
p < .0001
Mean signal intensity normalized to MT-length [a.u.]
Ase1
Ase1+Slk19
Stu1 signal intensity
p < .0001
Stu1
Stu1+Slk19

Combining our in vivo and in vitro data, we therefore suggest that Slk19 facilitates a protein interaction network that amplifies the levels of Ase1 and Stu1 above their basic levels and thus enhances MT cross-linking and rescue activity at the ipMT overlaps of metaphase spindles (Figure 8D).

DISCUSSION

We aimed to understand the role of Slk19 in the formation of the mitotic spindle of *S. cerevisiae* in prometaphase and its stabilization in metaphase. A protein that supports spindle formation might exert its role by affecting MT dynamics or imposing motor activity. However, Slk19 harbors no known domain that would suggest such functions. Alternatively, a protein may contribute to spindle formation by stabilizing MT alignment by MT cross-linking. However, we found that Slk19 cannot localize to the spindle per se. Rather, it depends on Stu1 and Ase1 for that. Also, Slk19 did not bind to MTs in vitro and thus could not cross-link MTs in vitro per se. Yet, Slk19 bound to MTs that were preloaded with Ase1 or Stu1. Additionally, Slk19 enhanced the cross-linking of MTs in vitro when added to the MTs in combination with Ase1 or Stu1. Furthermore, in the absence of Slk19, the localization of Ase1 and Stu1 at metaphase spindles was clearly decreased in vivo and the addition of Slk19 to Ase1 and Stu1 amplified the binding of these proteins to MTs in vitro. Some of these effects might be explained by altered Ase1 and Stu1 activities due to conformational changes induced by Slk19 interaction. In particular, the finding that Slk19 enhances cross-linking by Ase1 somewhat more than by Stu1 might indicate that Slk19 affects Ase1's cross-linking activity also through allosteric effects. However, the simplest (and not necessarily exclusive) explanation as to how Slk19 may stabilize spindles appears to be that Slk19 recruits additional Ase1 and Stu1 to the spindle and thus enhances MT cross-linking (Ase1 and Stu1) and MT stabilization (MT rescue activity of Stu1) (Figure 8D). Thus, although Slk19 has none of these activities itself, it contributes to both. Slk19 has been described to form homotetramers (De Wulf *et al.*, 2003). Slk19 therefore might facilitate the formation of a network that includes the homodimer (Schuyler *et al.*, 2003) Ase1 and the homodimer (Funk *et al.*, 2014) Stu1. Since this network should allow sufficient spindle flexibility, one may even speculate that the Slk19/Ase1/Stu1 network could be governed by forces as described for phase separation events (Alberti *et al.*, 2019). This idea could be supported by the observation that the Slk19-Ase1 interaction is apparently weak and the fact that Slk19 contains predominantly cc regions, one of the protein sequences that can promote phase separation effects (Alberti *et al.*, 2018). Compromising this network by interfering with Slk19's spindle function should increase MT instability and reduce MT cross-linking and consequently result in fewer overlaps of ipMTs. This is in agreement with the occurrence of an increased number of unaligned nrMTs in Δ*slk19* and *slk19*Δ*cc1* cells (Figure 3A). Furthermore, the centered appearance of ipMT overlaps in metaphase-arrested *WT* cells, as deduced from Ase1, Stu1, and Slk19 localization, may reflect the average of all MT overlaps in these cells. However, for instance, if cells form only one ipMT overlap, this overlap may frequently appear as acentric, particularly when MT dynamics is increased. Thus, the acentric localization of Ase1 in metaphase-arrested Δ*slk19* or *slk19*Δ*cc1* cells (Figure 6, C and D) may indicate a decreased number of overlaps and/or highly dynamic ipMTs. This is also in agreement with the reduced tubulin signal observed at the center of Δ*slk19* or *slk19*Δ*cc1* spindles (Figure 6, A and B). In contrast to Ase1, the localization of Stu1 exhibited no (centric or acentric) maximum in metaphase-arrested Δ*slk19* and *slk19*Δ*cc1* cells (Figure 6, C and D). One possible explanation might be that the Stu1 levels at ipMT overlaps of these cells are too low to exceed Stu1 levels at the remaining spindle and KTs. Another more attractive possibility is that Stu1 localization to MT overlaps in *WT* cells is favored over general MT binding because it is recruited to the overlaps by Slk19. It is intriguing that expression of Stu1ΔCL can rescue most of the metaphase spindle phenotypes observed in cells with defective Slk19 spindle localization and even in Δ*ase1* cells; *stu1ΔCL* cells exhibit longer kMTs and longer ipMTs than *WT* cells (Funk *et al.*, 2014). Thus, Stu1ΔCL may have enhanced MT rescue or even cross-linking activity in comparison to *WT* Stu1, albeit it is not clear how this is achieved. This may compensate for any reduced levels of Stu1 at the spindle in Δ*slk19* cells. In addition, due to the longer kMTs of *stu1ΔCL* cells, they exhibit a shorter distance between the KT clusters despite having longer ipMTs (Funk *et al.*, 2014). Thus, there is probably less tension at *stu1ΔCL* KTs and thus less force to withhold by the ipMTs. Could Slk19 (and Ase1) be needed only when spindles have to withhold the tension created in *WT* cells? In this context it is intriguing that Slk19 in Spc105-depleted cells not only fails to localize to KTs but also that its localization to the metaphase spindle is increased (Figure 1B). A reason for this might be that additional Slk19 is available when its KT localization is prevented. On the other side, spindle localization of Slk19 is also increased in cells that express Stu1ΔTOGL1, although Slk19 still localizes to the KTs in these cells (Supplemental Figure S1, A and B). Both Spc105-depleted cells and Stu1ΔTOGL1-expressing cells exhibit kMTs that are shorter and inter-KT cluster distances that are larger than that of *WT* cells (Supplemental Figure S1C). Thus, there is most likely higher tension at the KTs of these cells and more stress for their ipMTs to withhold this tension. The fact that an increased spindle localization of Slk19 correlates with this situation might indicate that spindle localization of Slk19 (and thus Ase1 and Stu1) is regulated by demand. Since Slk19 has been postulated to contribute to the elasticity of centromeric chromatin (Zhang *et al.*, 2006), overstretching of centromeric chromatin might also explain the phenotype of Spc105-depleted cells (with defective KT localization of Slk19). However, one would rather expect an increase in the pole to pole distance under these circumstances. Yet the opposite is the case. Furthermore, it has not been shown that Slk19 that localizes to KTs via Spc105 affects the centromeric chromatin. Rather, it was suggested (Zhang *et al.*, 2006) that Slk19 interacts with the cohesin Scc1. We therefore speculate that

FIGURE 7: Slk19 amplifies the MT binding of Ase1 and Stu1 in vitro. (A) Purified proteins used in the in vitro experiment, as revealed by SDS–PAGE and Coomassie staining. Black arrowheads mark the full-length proteins, the green arrowhead a naturally occurring cleavage product of Slk19 (Sullivan *et al.*, 2001) and red arrowheads Ase1 carrying two or one mCherry domains. An asterisk indicates IgG. (B–D) Stabilized and immobilized MTs were incubated with purified proteins and analyzed as indicated. Bars, 10 µm. (B) Slk19 does not bind to MTs in vitro. (C) Ase1 and Stu1 confer MT binding of Slk19 in vitro. MTs preloaded with Ase1 or Stu1 were subsequently incubated with Slk19 proteins. (D) Slk19 increases the binding of Ase1 and Stu1 to MTs in vitro. Where indicated, MTs were incubated with premixed Ase1 and Slk19 or Stu1 and Slk19. (E) Quantification of MT binding of Ase1 and Stu1. Statistics see Supplemental Table S4. The SD of two independent experiments is shown.

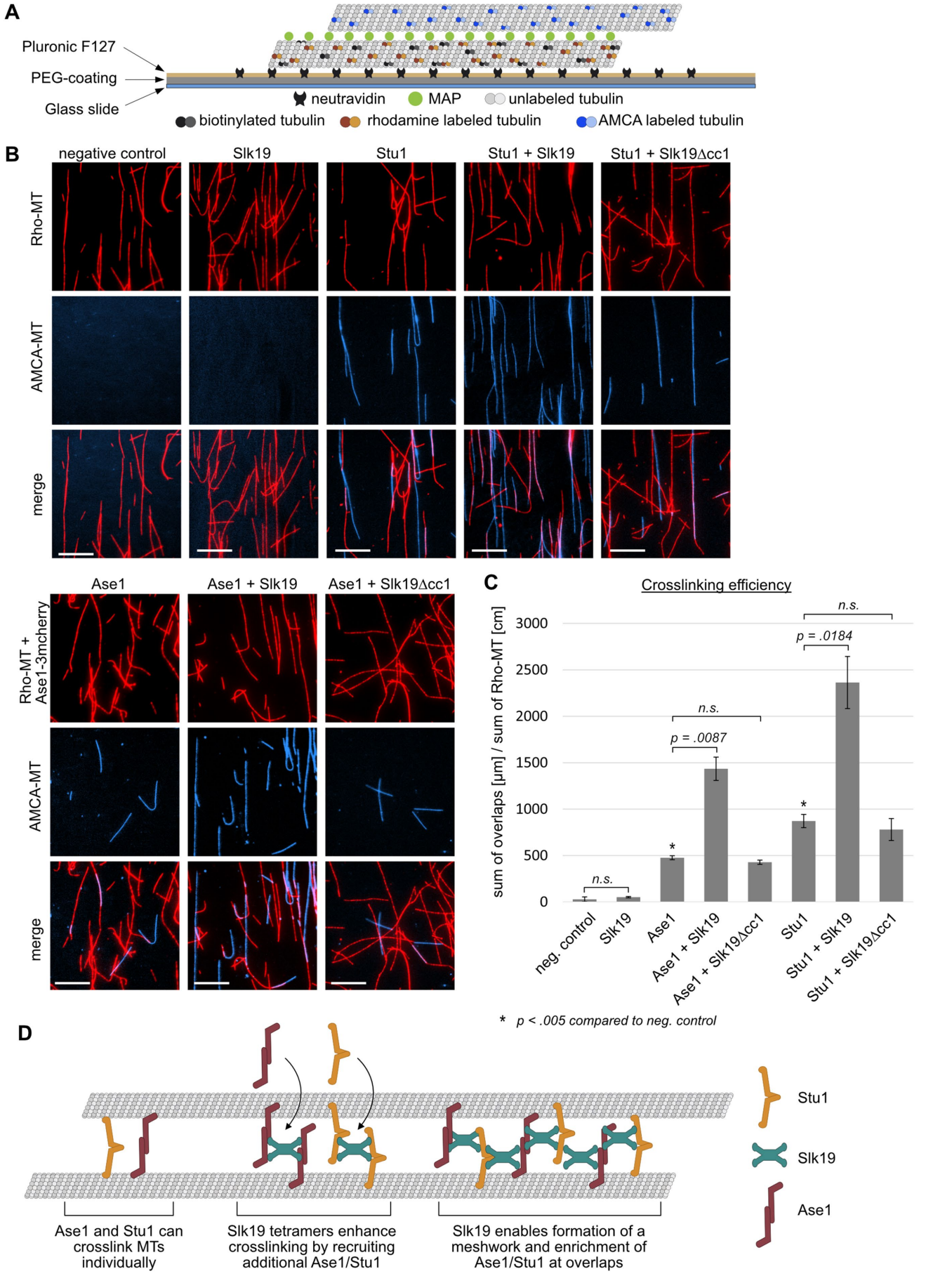
A
Pluronic F127
PEG-coating
Glass slide
neutravidin
MAP
unlabeled tubulin
biotinylated tubulin
rhodamine labeled tubulin
AMCA labeled tubulin
B
negative control
Slk19
Stu1
Stu1 + Slk19
Stu1 + Slk19Δcc1
Rho-MT
AMCA-MT
merge
Ase1
Ase1 + Slk19
Ase1 + Slk19Δcc1
Rho-MT + Ase1-3mcherry
AMCA-MT
merge
C
Crosslinking efficiency
sum of overlaps [µm] / sum of Rho-MT [cm]
3000
2500
2000
1500
1000
500
0
n.s.
p = .0184
n.s.
p = .0087
n.s.
*
*
neg. control
Slk19
Ase1
Ase1 + Slk19
Ase1 + Slk19Δcc1
Stu1
Stu1 + Slk19
Stu1 + Slk19Δcc1
* p < .005 compared to neg. control
D
Stu1
Slk19
Ase1
Ase1 and Stu1 can crosslink MTs individually
Slk19 tetramers enhance crosslinking by recruiting additional Ase1/Stu1
Slk19 enables formation of a meshwork and enrichment of Ase1/Stu1 at overlaps

the shortening of kMTs in Spc105-depleted cells is due to the absence of KT-localized Stu1 because Spc105 is essential to localize Stu1 to unattached KTs (Kolenda *et al.*, 2018). Since it is required to maintain kMT stability (Funk *et al.*, 2014), the absence of Stu1 would shorten kMTs and thus indeed increase tension at the KTs. The fact that cells expressing Stu1ΔTOGL1 exhibit a similar phenotype as the Spc105-depleted cells supports this assumption. Clearly further research is required to clarify these points.

Slk19 has been suggested to have a FEAR-independent function for the anaphase spindle because *slk19Δcc6+7* cells exhibit unaltered FEAR signaling but reduced MT overlaps in the spindle midzone (Havens *et al.*, 2010). Slk19Δcc1, like Slk19Δcc6+7, fails to localize to the spindle midzone in anaphase (Figure 2E). Thus, the ideas presented here for Slk19's role in metaphase could also apply to the spindle midzone in anaphase. On the other side, the D4 domain (Figure 1C) of Stu1 facilitates midzone localization independent of Stu1's MT binding domain or the CL domain (Funk *et al.*, 2014). Additionally, the dephosphorylation of Ase1 in anaphase directs other proteins like Cin8 to the midzone (Khmelinskii *et al.*, 2007). Thus, a Slk19 supported network of midzone proteins may exist, but it is likely to be more complex than in metaphase.

Alp7, the closest Slk19 homolog in *Schizosaccharomyces pombe*, also stabilizes ipMTs overlaps (Sato *et al.*, 2004). However in contrast to Slk19, Alp7 can bind to MTs per se and bundles MTs in vitro (Thadani *et al.*, 2009). Thus, Alp7 and Slk19 seem to contribute to similar spindle functions, but Alp7 apparently does it in a more direct way than Slk19. Alp7 localizes to KTs via a C-terminal transforming acid cc-containing (TACC) domain (Tang *et al.*, 2013). The Pfam database (http://pfam.xfam.org/) places a TACC domain also at the C-terminus of Slk19 overlapping cc6 and cc7, the Slk19 region that is required and sufficient for KT localization. Thus, Slk19 and Alp7 apparently use similar structural entities to bind to KTs. Alp7 at the KT forms a complex with Alp14, a XMAP215 MT polymerase (Tang *et al.*, 2013). The corresponding *S. cerevisiae* ortholog, Stu2, has been shown to facilitate tension sensing at the KT (Miller *et al.*, 2016). It is not known whether Stu2 interacts with Slk19. However, it appears interesting in the context that the amount of Slk19 spindle localization appears to correlate with the tension at KTs (see above).

Stu1 and Slk19 are sequestered at unattached KTs in order to facilitate the formation of nrMTs that capture these unattached KTs (Kolenda *et al.*, 2018). The removal of Stu1 strongly compromises the spindle, thus providing free tubulin for the formation of these nrMTs. Although they can grow far beyond the spindle region, these nrMTs might still be preferentially aligned along the spindle axes if Slk19 promotes Ase1 recruitment at the spindle. However, when Slk19 is sequestered at unattached KTs together with Stu1, dynamic stability and alignment are altered at the same time and this may allow the formation of MTs that span the nucleus in a truly random way. Thus, by shedding light on Slk19's role in metaphase spindle formation, we also may better understand why Slk19 is sequestered at unattached KTs when capturing is vital.

MATERIALS AND METHODS

Strain and plasmid construction

Genotypes of all yeast strains and plasmids are listed in Supplemental Tables S1 and S2. All used yeast strains are derivatives of YPH499. Tagging of endogenous genes, promoter replacements, and gene deletions were performed by PCR-mediated integration using sequences from pYM1, pYM2, pYM28, and pME1600. Protein depletion was performed by the auxin-induced degradation (AID) system (Nishimura *et al.*, 2009) using the plasmids pMK43, pME1595, and pJO1610. OsTIR1 was integrated into the *ADE2* locus using plasmid pVS1453 or pME1624. To produce strains harboring the *STU1* deletion construct stu1ΔCL, the construct was integrated into the endogenous STU1 locus using pVS1346 or into the LYS2 locus using pCF1498. *SLK19* deletion constructs were created by PCR or overlap-PCR. All *SLK19* deletion constructs are under the control of the endogenous *SLK19*-promoter and carry a FLAG-tag at the N-terminus, a SV40 nuclear localization signal at the C-terminus and optionally a GFP-tag at the C-terminus. The *SLK19* constructs were integrated into the *LYS2* locus of the respective yeast strain. The plasmids used for the transformation of the indicated yeast strains are listed in Supplemental Table S3.

Fluorescence microscopy

For live-cell imaging of yeast cells, a life science imaging station (CellR; Olympus) with an Olympus IX 81 motorized inverted fluorescence microscope, an Olympus MT20 illumination device including a 150 W Xenon arc burner, a Plan-Apochromat objective with a numerical aperture of 1.4 and 100× magnification in combination with IMMOIL-F30CC immersion oil (Olympus), and a charge-coupled device camera (ORCA-ER model C4742-80-12AG; Hamamatsu Photonics) was operated by the Olympus xCellence software. Images had 1344 × 1024 pixels (width × height), a scale of 15.625 pixels/µm, and a bit depth of 16 bit. Yeast cells were washed three times with water and resuspended in NFM (0.9 g/l KH_2PO_4, 0.23 g/l K_2HPO_4, 0.5 g/l $MgSO_4$, 3.5 g/l $(NH_4)_2SO_4$, 20 g/l glucose or galactose as carbon source, 0.79 g/l Complete Supplement Mixture (CSM, from Qbiogene), 0.5 mg/l β-alanine, 0.2 mg/l thiamine HCl, 3.0 mg/l D-pantothenic acid calcium salt, 2.0 mg/l inositol, 0.4 mg/l biotin, and pH adjusted to 5.5–6 with KOH). Seven z-stacks with a distance of 0.43 µm were acquired and projected. Imaging of in vitro MT assays was performed in BRB80 buffer (80 mM PIPES, pH 6.8/KOH, 1 mM $MgCl_2$, 1 mM EGTA, pH 6.8/KOH) supplemented with 0.13% methylcellulose, 50 mM KCL, 20 µM taxol, 2 mM dithiothreitol (DTT), 45 mM glucose, 0.4 mg/ml glucose oxidase (Sigma-Aldrich), 0.07 mg/ml catalase (Sigma-Aldrich), and 0.7 mg/ml β-casein (referred to as imaging buffer). For imaging of MTs, one z-stack was acquired. Fluorophores used were CFP, GFP, mCherry, rhodamine, and AMCA.

Image processing, analysis, and quantifications

Image processing was performed with the image processing package Fiji (ImageJ) including the projection of z-stacks, adjustments of brightness, and contrast of each color channel.

FIGURE 8: Slk19 enhances the cross-linking of MTs by Ase1 or Stu1 in vitro. (A) Experimental setup, modified from (Funk *et al.*, 2014). (B) As illustrated in A, stabilized MTs were immobilized, incubated with the indicated proteins (Figure 7A), and subsequently incubated with mobile MTs. Where indicated, Slk19 constructs were applied premixed with Stu1 or Ase1. Bars, 10 µm. (C) Quantification of colocalization (overlaps) of immobile and mobile MTs (cross-linking efficiency). The SD of two independent experiments is shown; n.s., not significant. Statistics see Supplemental Table S4. (D) Model depicting how Slk19 may support the cross-linking and stability of metaphase ipMTs. See *Discussion* for further explanation.

Plot profiles (gray value plotted against distance in microns) were collected for each color channel with the "Plot Profile" feature of Fiji. For longitudinal RGB plots (Figures 1B and 6, A and C; Supplemental Figure S1A), the signal intensities of indicated proteins were measured along the complete metaphase spindle, as defined by the distance between two SPBs (Figure 1B) or by the Tub1-CFP signal, plus 0.4 µm on each side of the spindle (Figure 6, A and C). These plots contain 45–51 measuring points (1 measuring point per pixel). The same spindle lengths were measured in each cell type for localization analysis (2-µm spindles in Figure 1B; 2.4-µm spindles in Figure 6, A and C; 3-µm spindles in Supplemental Figure S1A). The minimum value of each individual curve (not part of spindle) was subtracted as background from all values of the individual curve (resulting in a lowest value $v_{min} = 0$ for each curve). Where indicated, mean value curves ($n \geq 16$) were obtained. The average of the mean value curves of two individual experiments and the corresponding standard deviations are shown where indicated. The exact number of measured cells is listed in Supplemental Table S4 (Statistics). For Figure 6C, data of individual cells were normalized to obtain values ranging from 0 to 1 (v_{min}-v_{max}) for each curve. For cross-section RGB plots (Figure 6B), the center of 1.6- to 2.6-µm spindles as defined by the Tub1-CFP signal was identified. A 2.5-µm line (40 measuring points) was extended symmetrically from the center, orthogonal to the spindle axes. The minimum value of each individual curve was subtracted as background from all values of the individual curve (resulting in $v_{min} = 0$). Mean value curves ($n > 80$) were obtained for each experiment representing the average Tub1-distribution at the metaphase spindle center. The average of the mean value curves of two individual experiments and the corresponding standard deviations for each measuring point are shown in Figure 6B. The exact number of measured cells is listed in Supplemental Table S4.

Lengths and signal intensities were measured using the line tool or appropriate geometric tools of the Fiji software, respectively, to select the region of interest. Signal intensities were corrected by background subtraction. Where indicated, the data were normalized to other measured entities and mean values were obtained. Western analysis in Figure 5D: the mean values were obtained from loading multiples of the whole-cell extract (WCE) as indicated. This also confirmed the linearity of the signal response. To determine the protein amounts in colloidal Coomassie-stained gels (Figure 7A), their signals were compared with that of a protein standard. Quantification of in vitro binding of Stu1 and Ase1 to MTs (Figure 7E): the signal intensity was measured at ~10-µm-long MT regions ($n > 100$) from 4 to 8 micrographs. Quantification of in vitro MT cross-linking (Figure 8C): the lengths of all immobilized rhodamine MTs observed in ≥5 micrographs were measured and added (cumulative length). The lengths of overlaps between the mobile AMCA-MTs and immobilized rhodamine MTs were measured and normalized to the cumulative length of rhodamine MTs.

In Supplemental Figure S1C, the spindle length was defined by the distance between two opposing SPBs, the KT-KT distance was measured as distance between two related KT clusters, and the kMT length was measured as distance between SPB and the associated KT cluster.

Yeast cell culturing

Yeast cells were grown exponentially in liquid cultures at 25°C at 180 rpm in a shaking incubator. Cycling cells were grown in YP medium (10 g/l yeast extract and 20 g/l peptone, supplemented with 100 mg/l adenine, 30 mg/l uracil, and 50 mg/l tryptophan) with 2% glucose as carbon source (Figure 2, B and E). Cells were synchronized in G1 phase by incubation with 200 ng/ml α-factor (Figures 2E and 3B) and were released from α-factor arrest after approximately 2 h (Figure 2E) or after 1.5 h (Figure 3B). For the G1 release, cells were washed with water and resuspended in YP medium containing 2% glucose. Cells with *CDC20* under the control of a *GAL1* promoter were grown in YP medium with 2% raffinose and 1% galactose. For metaphase arrest, cells were shifted to YP medium with 2% glucose for 3.5 h (Figures 1A, 2, C and D, and 4A; Supplemental Figures S1, B and C, and S2). Cells were analyzed in NFM medium containing 2% glucose. Cells with *CDC20* under the control of a *MET25* promoter were grown in synthetic complete medium lacking methionine (6.7 g/l yeast nitrogen base without amino acids, 0.7 g/l CSM double drop-out -Met -Trp [from Formedium], 100 mg/l adenine, and 50 mg/l tryptophan) with 2% glucose. For metaphase arrest, cells were shifted to YP medium with 2% glucose and 2 mM methionine for 3.5 h (Figures 1A, 2, C and D, 3A, and 4A) or 4.5 h (Figure 5A; Supplemental Figure S1, A–C). Cells were analyzed in NFM medium containing 2% glucose and 2 mM methionine. For depletion of *IAA17*-tagged proteins, cells expressing OsTIR1 were shifted to YP medium supplemented with 1 mM indole acetic acid (IAA) and incubated for 3.5 h (Figures 1A, 2D, and 4A; Supplemental Figures S1, B and C, and S2). Cells were analyzed in NFM medium containing 2% glucose and 1 mM IAA.

Coimmunoprecipitation

Anti-FLAG M2 magnetic beads (Sigma-Aldrich) were used. The experiments in Figure 2B were performed as described (Funk *et al.*, 2014). For the pulldown of Slk19-9Myc by 5xFLAG-tagged Stu1 or Stu1ΔCL (Figure 4C), cells were resuspended in 4 µl/OD BH0.10$^+$ (BH0.10: 25 mM HEPES, pH 8.0, 2 mM $MgCl_2$, 150 mM KCl, 10% glycerol, 0.1 mM EDTA, pH 8.0, 0.5 mM EGTA, pH 8.0, 0.1% NP.40 with 2 mM DTT, 0.4 mM phenylmethylsulfonyl fluoride [PMSF], 20 µg/ml chymostatin, 20 µg/ml leupeptin, and 20 µg/ml pepstatin) supplemented with 2 mM β-glycerol phosphate disodium salt, 1 mM sodium pyrophosphate, 5 mM sodium fluoride, 0.1 mM vandate, 0.1 µM microcystin (lysis buffer), and frozen as small droplets. The frozen droplets were lysed by grinding within a precooled mortar and pestle. The procedure after the lysis was performed as described (Funk *et al.*, 2014). Proteins were eluted by incubating the beads at 25°C for 25 min at 900 rpm on a shaker with 250 µg/ml FLAG-peptide (Caslo ApS) in BH0.10$^+$.

WCEs and Western blot analysis

WCEs of metaphase-arrested cells (Figure 5C), were prepared as described (Hecht and Grunstein, 1999) and samples were quantified by a Bradford assay (Serva). The WCE samples were loaded on a precast SDS–PAGE gradient gel (4–20% Mini-PROTEAN TGX, Bio-Rad Laboratories) (Figure 5C) or on an 8% SDS–PAGE gel (Supplemental Figure S2).

Primary antibodies were used as indicated: rabbit anti-GFP antibody (1:2000 dilution) (Figure 2B; Supplemental Figure S2), mouse anti-FLAG-horseradish peroxidase (HRP) monoclonal antibody (1:2000 dilution; from Sigma-Aldrich) (Figures 2B and 4C), mouse anti-Myc monoclonal antibody (1:1500 dilution; from Sigma-Aldrich) (Figures 4C and 5C), and rabbit anti-Arc1 antibody (1:100000 dilution). The following secondary antibodies were used: goat α-rabbit-HRP (1:10000 dilution; from Sigma-Aldrich) (Figure 2B; Supplemental Figure S2), goat anti-mouse-HRP (1:10000 dilution; from Sigma-Aldrich) (Figure 4C), Alexa-Fluor 680

goat α-mouse, and Alexa-Fluor 680 goat α-rabbit polyclonal antibodies (1:10000; Invitrogen) (Figure 5C). Western blot analysis was performed using chemiluminescent detection (ECL solutions from Biological Industries) (Figures 2B, and 4C; Supplemental Figure S2) and for quantitative analyses the LI-COR Odyssey CLx Imaging System with the Image Studio Software (LI-COR Biosciences) was used (Figure 5C). Signal quantification was performed using the Fiji software.

Chromatin Immunoprecipitation (ChIP) assays and quantitative PCR

ChIP assays and quantitative PCR reactions were performed as described (Funk *et al.*, 2014). The quantitative PCR was performed in the StepOnePlus Real-Time PCR System including the StepOne Software (Applied Biosystems). Inputs were diluted 1:100 (analyzed as controls), and IP probes were diluted 1:5. The following primers and probes were used: Pho5-forward primer, 5′-GAATAGGCAATCTCTAAATGAATCGA-3′; Pho5-reverse primer, 5′-GAAAACAGGGACCAGAATCATAAATT-3′; Pho5-probe, 5′-ACCTTGGCACTCACACGTGGGACTAGC-3′; Cen3-forward primer, 5′-CCTTCCGCTTATAGTACAGTACCTA-3′; Cen3-reverse primer, 5′-TTCAATGAATAGCTTTCTGTGGA-3′; Cen3-probe, 5′-CGATCAGCGCCAAACAATATGGAA-3′ (Thermo Fisher Scientific). The amplification temperature was 60°C. The normalized enrichment of centromeric (*CEN3*) over non-centromeric DNA (*PHO5*) was calculated (*WT* was set to 100%).

Protein purifications for MT binding assays

FLAG-tagged proteins were purified from *S. cerevisiae*. Slk19 and Slk19Δcc1 were expressed from the endogenous *SLK19* promoter and Ase1 from the *GAL1* promoter (4 h, 2% galactose) while cells were arrested in metaphase. Stu1 was expressed from the *GAL1* promoter (5 h, 2% galactose). A dry cell pellet, frozen in liquid nitrogen, was ground by a Cryomill (2 × 1 min with frequency 30 s^{-1}) for cell lysis. After cell lysis, cells were resuspended in 1 µl/OD lysis buffer. The lysate was clarified two times at 20817 × *g* for 30 min at 4°C. The supernatant was incubated for 3 h under constant rotation at 4°C with α-FLAG antibody (Sigma-Aldrich) bound to protein G Dynabeads (Invitrogen). The beads were washed six times with BH0.10 buffer containing 200 mM PMSF and 2 mM DTT. The proteins Stu1 and Slk19Δcc1 were eluted by incubating the beads at 25°C for 25 min at 900 rpm with 250 µg/ml FLAG-peptide (Caslo ApS) in $BH0.10^+$. Slk19 was eluted identical to Stu1, with the exception that the KCl concentration was increased to 250 mM. Ase1 was eluted by incubating the beads at 25°C for 10 min at 900 rpm with 250 µg/ml FLAG-peptide (Caslo ApS) in 20 mM glycine, pH 2.5, buffer (prepared as $BH0.10^+$ but without 25 mM HEPES). Subsequently, the elution was neutralized to pH 7 with 25 mM HEPES.

In vitro MT binding and cross-linking assay

Cleaning, hydroxylation, amino-silanization, and PEGylation of glass slides. Cover slips used for MT in vitro assays (24 mm × 24 mm and 24 mm × 60 mm) were cleaned, hydroxylated, silanized, and PEGylated before usage (as described in "Slide Cleaning and Preparation Protocol 2.5" from Hoskins laboratory, University of Wisconsin-Madison, last modified 2016, accessed 2021, https://hoskins.biochem.wisc.edu/files/Data_Upload/2017-03-29_1413_Slide%20Prep%202_5.pdf). Flow chambers assembled with double-sided tape were PEGylated for 1 h in a humid chamber with a mixture of equal volumes of 5 mg/ml Biotin-PEG-NHS and 500 mg/ml MeO-PEG-NHS (both 5000 Da, Iris Biotech, dissolved in 0.1 M sodium hydrogen carbonate [$NaHCO_3$], pH 7.5).

Neutravidin coating and blocking of unspecific binding sites. Flow chambers were washed with 200 µl H_2O and 200 µl phosphate-buffered saline (PBS) and subsequently incubated with 30 µl of 5 mg/ml neutravidin (Invitrogen, dissolved in PBS) for 20 min as adapted from Mieck *et al.* (2015). Unbound neutravidin was removed by washing with 50 µl PBS before the glass surface was passivated for 5 min with 1% Pluronic F-127 solution (Invitrogen, dissolved in PBS) (Mieck *et al.*, 2015). Subsequently, each chamber was washed with 40 µl $BRB80^+$ buffer (BRB80 supplemented with 2 mM DTT, 50 mM KCl, and 20 µM taxol).

MT polymerization and pelleting. Fluorescently labeled MTs were polymerized and pelleted through a BH0.40 cushion (as described in (Funk *et al.*, 2014), and the pellet was resuspended in $BRB80^+$ buffer and infused into the chamber. After 15 min incubation in the dark, unbound MTs were removed from the chamber by perfusion with 30 µl MC/C buffer (0.13% methylcellulose and 0.7 mg/ml β-casein resuspended in $BRB80^+$ buffer). Unspecific binding sites were blocked by incubating in MC/C buffer for 5 min before adding the protein(s).

Protein binding analysis. Purified proteins were centrifuged for 10 min at 4°C and 20817 × *g* before diluting them in MC/C buffer to the respective concentration with a volume of 20 µl (final 60 mM KCl). For Figure 7, B and C, Ase1, Stu1, and Slk19 were used in a final concentration of 14.5, 10, and 20 nM, respectively. For Figure 7D, Ase1, Stu1, and Slk19 were used in a final concentration of 2.5, 5, and 20 nM, respectively. Each protein or protein mixture was incubated for 15 min and subsequently unbound protein was washed off with 30 µl imaging buffer.

MT cross-linking analysis. For the MT cross-linking assays (Figure 8B), Slk19, Ase1, and Stu1 were used in a final concentration. of 10, 7.2, and 5 nM, respectively. As negative control (no protein), 20 µl of MC/C buffer was used (final 60 mM KCl). For analysis of cross-linking ability, 10 µl unbiotinylated AMCA-MTs were infused into each flow chamber. After 10 min incubation, un-cross-linked MTs were removed by washing the chamber with 60 µl imaging buffer.

Statistical analyses

The significance level $\alpha = 0.05$ was chosen for all statistical tests. A two-tailed Fisher's exact test was performed to analyze whether defined phenotypes (categorical data) were observed with significantly different frequency between two independent groups (Jeremy Stangroom, Social Science Statistics Home Page, accessed 2021, http://www.socscistatistics.com/tests/fisher/default2.aspx). For comparison of two independent groups with several different phenotypes (categorical data), the $\chi 2$-test was used instead of Fisher's exact test (Jeremy Stangroom, Social Science Statistics Home Page, https://www.socscistatistics.com/tests/chisquare2/default2.aspx, accessed 2021). A two-tailed unpaired *t* test was used to analyze whether the mean values (metric data) from two independent groups differ significantly (Jeremy Stangroom, Social Science Statistics Home Page, https://www.socscistatistics.com/tests/studentttest/default2.asp, accessed 2021).

ACKNOWLEDGMENTS

We thank Marina Pelzl for excellent technical assistance and for reading the manuscript. This work was supported by a grant from the Deutsche Forschungsgemeinschaft.

REFERENCES

Alberti S, Gladfelter A, Mittag T (2019). Considerations and challenges in studying liquid-liquid phase separation and biomolecular condensates. Cell 176, 419–434.

Alberti S, Saha S, Woodruff JB, Franzmann TM, Wang J, Hyman AA (2018). A user's guide for phase separation assays with purified proteins. J Mol Biol 430, 4806–4820.

Bieling P, Telley IA, Surrey T (2010). A minimal midzone protein module controls formation and length of antiparallel microtubule overlaps. Cell 142, 420–432.

De Wulf P, McAinsh AD, Sorger PK (2003). Hierarchical assembly of the budding yeast kinetochore from multiple subcomplexes. Genes Dev 17, 2902–2921.

Faust AM, Wong CC, Yates JR 3rd, Drubin DG, Barnes G (2013). The FEAR protein Slk19 restricts Cdc14 phosphatase to the nucleus until the end of anaphase, regulating its participation in mitotic exit in Saccharomyces cerevisiae. PLoS One 8, e73194.

Funk C, Schmeiser V, Ortiz J, Lechner J (2014). A TOGL domain specifically targets yeast CLASP to kinetochores to stabilize kinetochore microtubules. J Cell Biol 205, 555–571.

Gillett ES, Espelin CW, Sorger PK (2004). Spindle checkpoint proteins and chromosome-microtubule attachment in budding yeast. J Cell Biol 164, 535–546.

Havens KA, Gardner MK, Kamieniecki RJ, Dresser ME, Dawson DS (2010). Slk19p of Saccharomyces cerevisiae regulates anaphase spindle dynamics through two independent mechanisms. Genetics 186, 1247–1260.

Hecht A, Grunstein M (1999). Mapping DNA interaction sites of chromosomal proteins using immunoprecipitation and polymerase chain reaction. Methods Enzymol 304, 399–414.

Hepperla AJ, Willey PT, Coombes CE, Schuster BM, Gerami-Nejad M, McClellan M, Mukherjee S, Fox J, Winey M, Odde DJ, *et al*. (2014). Minus-end-directed Kinesin-14 motors align antiparallel microtubules to control metaphase spindle length. Dev Cell 31, 61–72.

Khmelinskii A, Lawrence C, Roostalu J, Schiebel E (2007). Cdc14-regulated midzone assembly controls anaphase B. J Cell Biol 177, 981–993.

Khmelinskii A, Roostalu J, Roque H, Antony C, Schiebel E (2009). Phosphorylation-dependent protein interactions at the spindle midzone mediate cell cycle regulation of spindle elongation. Dev Cell 17, 244–256.

Kolenda C, Ortiz J, Pelzl M, Norell S, Schmeiser V, Lechner J (2018). Unattached kinetochores drive their own capturing by sequestering a CLASP. Nat Commun 9, 886.

Kornakov N, Mollers B, Westermann S (2020). The EB1-Kinesin-14 complex is required for efficient metaphase spindle assembly and kinetochore bi-orientation. J Cell Biol 219.

Lianga N, Dore C, Kennedy EK, Yeh E, Williams EC, Fortinez CM, Wang A, Bloom KS, Rudner AD (2018). Cdk1 phosphorylation of Esp1/Separase functions with PP2A and Slk19 to regulate pericentric Cohesin and anaphase onset. PLoS genetics 14, e1007029.

London N, Biggins S (2014). Mad1 kinetochore recruitment by Mps1-mediated phosphorylation of Bub1 signals the spindle checkpoint. Genes Dev 28, 140–152.

London N, Ceto S, Ranish JA, Biggins S (2012). Phosphoregulation of Spc105 by Mps1 and PP1 regulates Bub1 localization to kinetochores. Curr Biol 22, 900–906.

Mieck C, Molodtsov MI, Drzewicka K, van der Vaart B, Litos G, Schmauss G, Vaziri A, Westermann S (2015). Non-catalytic motor domains enable processive movement and functional diversification of the kinesin-14 Kar3. Elife 4.

Miller MP, Asbury CL, Biggins S (2016). A TOG protein confers tension sensitivity to kinetochore-microtubule attachments. Cell 165, 1428–1439.

Mittal P, Chavan A, Trakroo D, Shah S, Ghosh SK (2019). Outer kinetochore protein Dam1 promotes centromere clustering in parallel with Slk19 in budding yeast. Chromosoma.

Nishimura K, Fukagawa T, Takisawa H, Kakimoto T, Kanemaki M (2009). An auxin-based degron system for the rapid depletion of proteins in nonplant cells. Nat Methods 6, 917–922.

Pagliuca C, Draviam VM, Marco E, Sorger PK, De Wulf P (2009). Roles for the conserved spc105p/kre28p complex in kinetochore-microtubule binding and the spindle assembly checkpoint. PloS one 4, e7640.

Petry S (2016). Mechanisms of mitotic spindle assembly. Annu Rev Biochem 85, 659–683.

Podolski M, Mahamdeh M, Howard J (2014). Stu2, the budding yeast XMAP215/Dis1 homolog, promotes assembly of yeast microtubules by increasing growth rate and decreasing catastrophe frequency. J Biol Chem 289, 28087–28093.

Richmond D, Rizkallah R, Liang F, Hurt MM, Wang Y (2013). Slk19 clusters kinetochores and facilitates chromosome bipolar attachment. Mol Biol Cell 24, 566–577.

Sato M, Vardy L, Angel Garcia M, Koonrugsa N, Toda T (2004). Interdependency of fission yeast Alp14/TOG and coiled coil protein Alp7 in microtubule localization and bipolar spindle formation. Mol Biol Cell 15, 1609–1622.

Saunders WS, Hoyt MA (1992). Kinesin-related proteins required for structural integrity of the mitotic spindle. Cell 70, 451–458.

Schuyler SC, Liu JY, Pellman D (2003). The molecular function of Ase1p: evidence for a MAP-dependent midzone-specific spindle matrix. Microtubule-associated proteins. J Cell Biol 160, 517–528.

Severin F, Habermann B, Huffaker T, Hyman T (2001). Stu2 promotes mitotic spindle elongation in anaphase. J Cell Biol 153, 435–442.

Stegmeier F, Visintin R, Amon A (2002). Separase, polo kinase, the kinetochore protein Slk19, and Spo12 function in a network that controls Cdc14 localization during early anaphase. Cell 108, 207–220.

Subramanian R, Wilson-Kubalek EM, Arthur CP, Bick MJ, Campbell EA, Darst SA, Milligan RA, Kapoor TM (2010). Insights into antiparallel microtubule crosslinking by PRC1, a conserved nonmotor microtubule binding protein. Cell 142, 433–443.

Sullivan M, Lehane C, Uhlmann F (2001). Orchestrating anaphase and mitotic exit: separase cleavage and localization of Slk19. Nat Cell Biol 3, 771–777.

Tang NH, Takada H, Hsu KS, Toda T (2013). The internal loop of fission yeast Ndc80 binds Alp7/TACC-Alp14/TOG and ensures proper chromosome attachment. Mol Biol Cell 24, 1122–1133.

Thadani R, Ling YC, Oliferenko S (2009). The fission yeast TACC protein Mia1p stabilizes microtubule arrays by length-independent crosslinking. Curr Biol 19, 1861–1868.

Winey M, Mamay CL, O'Toole ET, Mastronarde DN, Giddings TH Jr, McDonald KL, McIntosh JR (1995). Three-dimensional ultrastructural analysis of the Saccharomyces cerevisiae mitotic spindle. J Cell Biol 129, 1601–1615.

Yin H, You L, Pasqualone D, Kopski KM, Huffaker TC (2002). Stu1p is physically associated with beta-tubulin and is required for structural integrity of the mitotic spindle. Mol Biol Cell 13, 1881–1892.

Zeng X, Kahana JA, Silver PA, Morphew MK, McIntosh JR, Fitch IT, Carbon J, Saunders WS (1999). Slk19p is a centromere protein that functions to stabilize mitotic spindles. J Cell Biol 146, 415–425.

Zhang T, Lim HH, Cheng CS, Surana U (2006). Deficiency of centromere-associated protein Slk19 causes premature nuclear migration and loss of centromeric elasticity. J Cell Sci 119, 519–531.